Theoretical investigation of the magnetic dynamics and superconducting pairing symmetry in α-$RuCl_3$

Wei Wang, Zhao-Yang Dong, Shun-Li Yu, and Jian-Xin Li*
National Laboratory of Solid State Microstructures and Department of Physics, Nanjing University, Nanjing 210093, China and Collaborative Innovation Center of Advanced Microstructures, Nanjing University, China
(Dated: August 30, 2018)

We study the spin-wave excitations in α-$RuCl_3$ by the spin-wave theory. Starting from the five-orbital Hubbard model and the perturbation theory, we derive an effective isospin-1/2 model in the large Hubbard (U) limit. Based on the energy-band structure calculated from the first-principle method, we find that the effective model can be further reduced to the $K-\Gamma$ model containing a ferromagnetic nearest-neighbor (NN) Kitaev interaction (K) and a NN off-diagonal exchange interaction (Γ). With the spin-wave theory, we find that the $K-\Gamma$ model can give magnetic excitations which is consistent with the recent neutron scattering experiments. Furthermore, to investigate various particle-hole excitations and possible superconducting pairing symmetry in the doped systems, we ignore the effects of the e_g orbitals and use the random-phase approximation. Our results show that the $J_{\text{eff}}=1/2$ picture is robust in the doped systems, and the d-wave pairing is the most favourable superconducting pairing symmetry.

I. INTRODUCTION

Currently, considerable attention has been attracted to exotic physics driven by the interplay of the spin-orbit coupling (SOC), crystal field and electronic correlation. Especially, in $4d$ or $5d$ transition metal materials, neither the Hubbard interaction U nor the SOC λ can solely lead to the insulating behavior. However, the interplay between U, λ and crystal field Δ could induce the so-called spin-orbit Mott insulator[1–3]. When d orbitals are subject to an octahedra crystal field circumstance, these states are split into a t_{2g} triplet and an e_g doublet. For the partially filled d^5 configuration, it is depicted by a single hole which has an effective orbital angular momentum $l=1$, related to effective angular momentum $\boldsymbol{J}_{\text{eff}}=\boldsymbol{s}-\boldsymbol{L}$, where $\boldsymbol{s}(\boldsymbol{L})$ is the spin(orbital) angular momentum. Thus, for large SOC, the t_{2g} multiplet is divided into a $J_{\text{eff}}=3/2$ quartet and a $J_{\text{eff}}=1/2$ Kramers doublet. Then, a moderate interaction U can open a Mott gap in the Kramers doublet due to its narrow band width. In particular, a significant consequence of $J_{\text{eff}}=1/2$ states in real materials is Heisenberg-Kitaev (HK) model, in which the Kitaev interaction is an unusual bond dependent exchange[4,5]. The pioneer examples are the $5d^5$-iridate compounds A_2IrO_3(A=Na,Li)[6–12] which contain honeycomb lattices with low-spin magnetic ions Ir^{4+} and the edge-sharing octahedral crystal field. But the fact that Ir ions have large neutron absorption cross-section hinders the neutron studies[6,7]. In addition, the trigonal distortions arouse the controversy about the concept of $J_{\text{eff}}=1/2$ picture for iridates[13].

Recently, α-$RuCl_3$ which is a $4d^5$ analogue of iridates was suggested as another candidate[14–16]. In contrast to iridates, $RuCl_6$ octahedra is much closer to cubic and layers are weakly coupled by van der Waals interactions. Even though the value of SOC is expected to smaller than that of $5d$ element, the intermediate SOC of Ru^{3+} combined with correlation effects in a narrow Ru^{3+} d band could also lead to the $J_{\text{eff}}=1/2$ picture[14,15,17–20]. Experimentally, due to stacking faults, two different crystalline symmetries have been reported in this compound, including both $P3_112$[15,17,21,22] ($P3$) and $C2/m$[16,23–25] ($C2$) space groups. The neutron scattering[15,16,20], X-ray diffraction[25] and heat capacity[14–16,22] measurements have pointed towards a zigzag type magnetic order at $T_{N1}\approx 14$ K and $T_{N2}\approx 8$ K which are associated with stacking faults. Moreover, above magnetic ordering temperature the broad continuum scattering is observed not only in inelastic neutron scattering (INS)[15,26] but also in Raman scattering[27], which suggests that α-$RuCl_3$ may realize Kitaev physics. The INS experiments[26] suggest that the Kitaev interaction is antiferromagnetic, but below T_{N1} a spin gap near M point is observed[15,26,28], which is not consistent with the theoretical results based on the HK model with an antiferromagnetic Kitaev interaction. Therefore, the HK model is not enough to depict the physics in α-$RuCl_3$. Moreover, many theoretical works suggested that the Kitaev interaction is ferromagnetic[29–31]. Besides, in previous work, the crystal field is expected to be large enough so that one can only take the t_{2g} manifold into account at low energies. However, the crystal field splitting Δ is estimated to be 2.2 eV from the XAS data[19,32], which is comparative to Hubbard U. Therefore, it is necessary to study the effect of crystal field Δ on the low energy behavior by including all of the five d orbitals.

In this paper, we derive a minimal effective exchange model where the first nearest neighbor (NN) Kitaev interaction is ferromagnetic by projecting the five-orbital Hubbard model onto the lowest Kramers doublet. By analysing the magnetic interactions, we find that the exchange between e_g and t_{2g} orbitals can enhance the NN ferromagnetic Kitaev interaction K_1 and off-diagonal exchange Γ_1, and reduce the NN ferromagnetic Heisenberg interaction J_1. We investigate the magnetic dynamics of this model which is consistent with the results of INS experiments[15,26,28] through the SU(2) spin wave theory. We further verify the validity of the minimal exchange

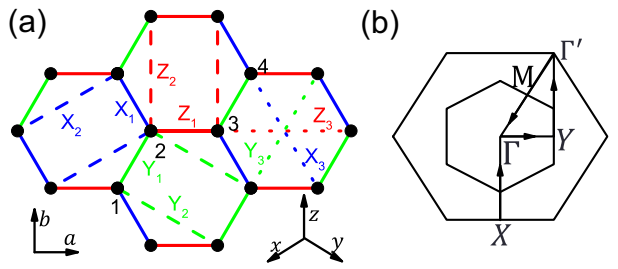

FIG. 1. (Color online)(a) Solid, dashed and dotted lines label first, second and third NN bonds on honeycomb lattice respectively. Red, green and blue colors depict the Z, Y and X bonds, respectively. a, b refer to the axes in honeycomb layer, while x, y, z are the cubic axes of the local octahedra. Sites within magnetic unit cell are labeled $1-4$. (b) Symmetry path $X-\Gamma-Y-\Gamma'-M-\Gamma$ is shown in reciprocal space.

model through the comparison to the spin wave excitations calculated based on the exchange model which contains the $J_{\rm eff}=1/2$ and $J_{\rm eff}=3/2$ states. Then, we investigate various particle-hole (PH) excitations and possible superconductivity in the doped systems with the random-phase-approximation (RPA) method. We find that the $J_{\rm eff}=1/2$ isospin fluctuations dominate over the fluctuations from other PH excitations, suggesting the robustness of the $J_{\rm eff}=1/2$ picture even in doped systems, and the most favorable superconducting state mediated by the isospin fluctuations has a d-wave pairing symmetry.

II. MAGNETIC DYNAMICS IN UNDOPED SYSTEMS

A. Minimal effective model

To investigate the magnetic dynamics in the parent compound of $\alpha-{\rm RuCl_3}$, we first construct an effective exchange model from the multi-orbital Hubbard model, which includes all of the five $4d$ orbitals of Ru^{3+}. The Hamiltonian of the multi-orbital Hubbard model can be written as

$$H=H_t+H_\triangle+H_{soc}+H_{int}. \tag{1}$$

The kinetic energy term H_t and crystal field $H_\triangle$ are expressed as

$$H_t=\sum_{ij,\sigma}\psi^\dagger_{i\sigma}\mathcal{T}_{ij}\psi^\dagger_{j\sigma} \tag{2}$$

and

$$H_\triangle=\sum_{ij,\sigma}\psi^\dagger_{i\sigma}h^\Delta_{ij}\psi^\dagger_{j\sigma}, \tag{3}$$

where $\psi^\dagger_{i,\sigma}=(d^\dagger_{i,z^2,\sigma},d^\dagger_{i,x^2-y^2,\sigma},d^\dagger_{i,yz,\sigma},d^\dagger_{i,xz,\sigma},d^\dagger_{i,xy,\sigma})$ with $d^\dagger_{i,m,\sigma}$ creating an electron of spin σ at site i in the orbital m. The parameters of $\mathcal{T}_{ij}$ and h^Δ for a tight-binding fit of the band structure based on the density-functional theory (DFT) are listed in the Appendix A. $H_{soc}=\sum_i\lambda\boldsymbol{L}_i\cdot\boldsymbol{s}_i$ is the electron spin-orbit interaction. The on-site Coulomb interaction H_{int} is given by

$$\begin{aligned}H_{int}=&\frac{1}{2}\sum_{imm'nn'}\sum_{\alpha\beta\mu\nu}\delta_{\alpha\nu}\delta_{\beta\mu}\{U\delta_{m=m'=n=n'}(1-\delta_{\alpha\beta})\\&+U'\delta_{mn'}\delta_{m'n}(1-\delta_{mm'})+J_H\delta_{mn}\delta_{m'n'}(1-\delta_{mm'})\\&+J'\delta_{mm'}\delta_{mn'}(1-\delta_{mn})(1-\delta_{\alpha\beta})\}\\&d^\dagger_{im\alpha}d^\dagger_{im'\beta}d_{in\mu}d_{in'\nu},\end{aligned} \tag{4}$$

where U (U') is the intra-orbital (inter-orbital) Coulomb interaction, J_H and J' are the Hund's coupling and the pairing hopping respectively. In this paper, we employ $U=U'+2J_H$ and $J_H=J'$.

Next, we consider the large U limit and derive an effective exchange model through the second-order perturbation approximation. In the perturbation theory, the total Hamiltonian of Eq. (1) is divided into two parts $H_0=H_{int}+H_{soc}+H_\Delta$ and $H_1=H_t$. Then we arrive at the effective Hamiltonian in a formal expression[33]

$$H_{\rm eff}=PH_1P+PH_1\frac{1}{E_0-H_0}(1-P)H_1P, \tag{5}$$

where the projection operator P projects states into the low-energy subspace with the eigenvalues E_0 of H_0.

In the limit $U\sim\Delta\gg t$ and $\lambda\gg\frac{t^2}{U}$, the local degrees of freedom are governed by the lowest two states, labelled by $|1\rangle$ and $|2\rangle$, which are many body states occupied by five electrons and become the $J_{\rm eff}=1/2$ Kramers doublet exactly when the crystal field Δ tends to infinity. By projecting $H_{\rm eff}$ into the subspace of the Kramers doublet with the projection operator $P=|1\rangle\langle1|+|2\rangle\langle2|$ and expanding the Hamiltonian matrix on each bond in the form of $S^\alpha_iS^\beta_j$, where isospin operator $\boldsymbol{S}=P\boldsymbol{J}_{\rm eff}P$ is the projection of the total effective angular momentum $\boldsymbol{J}_{\rm eff}$ and satisfies the commutation relation $[S^\alpha,S^\beta]=i\epsilon^{\alpha\beta\gamma}S^\gamma$ ($\epsilon^{\alpha\beta\gamma}$ is Levi-Civita symbol) exactly if $\Delta=\infty$, we can obtain a effective model involving exchange interactions up to the third nearest neighbors (NN),

$$\begin{aligned}H_{\rm eff}=&\sum_{\langle ij\rangle\in\gamma(\alpha\beta)}[J_1^\gamma\boldsymbol{S}_i\cdot\boldsymbol{S}_j+K_1^\gamma S_i^\gamma S_j^\gamma+\Gamma_1^\gamma(S_i^\alpha S_j^\beta+S_i^\beta S_j^\alpha)\\&+\Gamma_1'^\gamma(S_i^\alpha S_j^\gamma+S_i^\beta S_j^\gamma+S_i^\gamma S_j^\beta+S_i^\gamma S_j^\alpha)]\\&+\sum_{\langle\langle ij\rangle\rangle\in\gamma}(J_2^\gamma\boldsymbol{S}_i\cdot\boldsymbol{S}_j+K_2^\gamma S_i^\gamma S_j^\gamma)\\&+\sum_{\langle\langle\langle ij\rangle\rangle\rangle\in\gamma}K_3^\gamma S_i^\gamma S_j^\gamma.\end{aligned} \tag{6}$$

Here, $\langle ij\rangle$, $\langle\langle ij\rangle\rangle$ and $\langle\langle\langle ij\rangle\rangle\rangle$ denote the first NN, second NN and third NN bonds respectively, where the second NN terms correspond to the triangular lattice HK

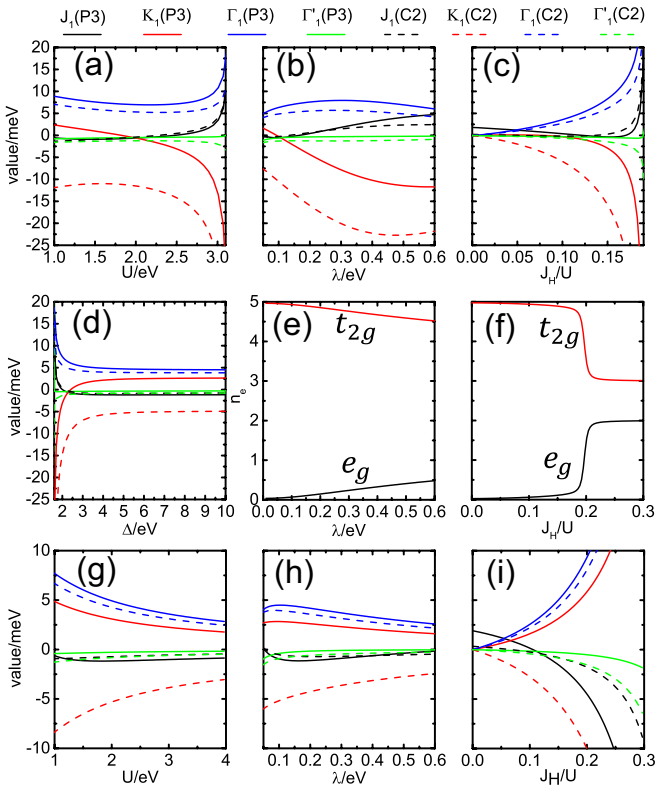

FIG. 2. (Color online) Dependence of the first NN interactions on the parameters for $C2$ case (dashed) and $P3$ case (solid). (a) U-dependence with $\Delta = 2.10$ eV, $\lambda = 0.14$ eV and $\frac{J_H}{U} = 0.14$. (b) λ-dependence with $\Delta = 2.10$ eV, $U = 2.31$ eV and $\frac{J_H}{U} = 0.14$. (c) $\frac{J_H}{U}$-dependence with $\Delta = 2.10$ eV, $U = 2.31$ eV and $\lambda = 0.14$ eV. (d) Δ-dependence with $U = 2.31$ eV, $\lambda = 0.14$ eV and $\frac{J_H}{U} = 0.14$. (g)-(i) with $\Delta = 210$ eV corresponding to (a)-(c). (e) and (f) show the number of electrons in Kramers doublet per site corresponding to (b) and (c) respectively. The black (red) line is e_g (t_{2g}) orbitals.

model[34]. γ represents the direction of each bond as shown in Fig. 1. For Z-type, X-type and Y-type bonds in Fig. 1, $(\alpha\beta)$'s are (xy), (yz) and (zx) respectively. J and K are the intensities of the Heisenberg and Kitaev interactions, Γ and Γ' are off-diagonal exchanges. The subscripts 1, 2 and 3 in J, K and Γ are used to indicate the first, second and third NN bonds respectively. In the case of $P3$ space group, the interactions are invariant for different directions due to the C_3 symmetry. However, for the low symmetric $C2$ space group, the interactions on the X and Y-bonds are equal but different from those on the Z-bonds. Moreover, in the case of $C2$ space group, J and Γ' on the X-type and Y-type bonds take the average values over the spin directions[29] to make them equal for all directions. As the signs of third NN diagonal hopping in t_{2g} orbitals are different (see Table.I which makes the third NN Heisenberg term is much smaller than the third NN Kitaev term), we only keep the K_3 term.

The exchange interaction parameters in Eq. (6) depend on the hopping integrals between various orbitals, the crystal field Δ, the SOC λ, the Hubbard interaction U and Hunds coupling J_H. The hopping integrals are determined from the first-principle calculations and the dependences of exchange interactions on Δ, λ, U and J_H are shown in Fig. 2. To simplify the comparison, the values of interactions are bond-averaged in the $C2$ case, so the superscript γ is omitted. As the second and third NN terms are small in contrast to the first NN term, we only exhibits the values of the first NN terms in Fig. 2. In Fig. 2 (a)-(c), we fix $\Delta = 2.1$ eV which is suitable for α-$RuCl_3$. To investigate the effect of the e_g orbital, we deliberate to choose an unrealistic large $\Delta = 210$eV and the results are shown in Fig. 2 (g)-(i) for a comparison. As shown in Fig. 2 (a), the magnitude of the exchange interactions has a trend to decrease and then increase with the increase of U. As U increases the gap between the Kramers doublet and other excitation states, the effective exchange interactions will decrease with U according to Eq. 5. In Fig. 2 (a), we fix the value of J_H/U, so the Hund's coupling J_H increases with U. For the $4d^5$ electron configuration, the Hund's coupling will decrease the energies of the excitations which contains a large weight of e_g orbitals, so the exchange interactions increase with J_H. Therefore, there is a competing relation between U and J_H in determining the exchange interactions. We can see this point more clearly in Fig. 2 (g), where the crystal filed Δ is set at a deliberate large value, so that the effect of the e_g orbitals is excluded and the effect of J_H is suppressed. In this case, all the exchange interactions decrease with U. In Fig. 2 (i), the large J_H/U induces the ferromagnetic J_1 interaction and enhances the values of the antiferromagnetic K_1 interaction in the $P3$ case, the ferromagnetic K_1 interaction in the $C2$ case, and the ferromagnetic Γ_1 interactions in both cases. The different signs of the K_1 interactions in two cases depend on the hoppings in the t_{2g} orbitals. The antiferromagnetic K_1 term in the $P3$ cases comes mainly from the direct hopping t_3 between the d_{xy} orbitals for the Z-bond. The K_1 term in the $C2$ case is attributed to the indirect hopping t_2 between t_{2g} orbitals via chlorine ions. However, when Δ is reduced to be comparable to the Hubbard U, as shown in panel (c), a large J_H leads to the ferromagnetic K_1 in the $P3$ case and the antiferromagnetic J_1 in both cases. It is also supported by the their Δ dependence. This is because a large J_H/Δ increases the mixing of the e_g and t_{2g} orbitals in the Kramers doublet, as shown in panel (f) where the number of electrons n_e in the e_g orbitals increases rapidly for $J_H/U > 0.19$. Moreover, by comparing Fig. 2 (c) with (i), we find that the $e_g - t_{2g}$ channels can enhance the magnitude of the Γ_1 and K_1 interactions. When the weight of e_g orbitals in the Kramers doublet increases rapidly, the values of interactions are divergent and the $J_{\text{eff}} = 1/2$ picture is no longer applicable. From the λ dependence as shown in Fig. 2 (b), (e) and (h), we can see that in the large Δ limit the values of interactions are suppressed with large λ owning to the enhancement of the gap between the $J_{\text{eff}} = 1/2$ and $J_{\text{eff}} = 3/2$ states, which is consistent

with previous work[29]. If Δ is reduced, the increase of λ results in the same effect as the increase of J_H/U, as seen in Fig. 2 (b) and (e). However, when λ is increased to 0.4 eV, the values of interactions increase slowly and even decrease. This is because the effect of the gap between the $J_{\rm eff}=1/2$ and$J_{\rm eff}=3/2$ states on interactions is greater than that of the e_g-t_{2g} channels.

In α-$RuCl_3$, $\Delta\approx 2.2$eV, $U=2\sim 3$eV and $\lambda=0.13\sim 0.15$eV[15,19,29,32,35], so we find that the leading exchange interactions are K_1 and Γ_1 terms according to the results in Fig. 2 and above discussions. Thus, a minimal model arises as,

$$H_{min}=\sum_{\langle ij\rangle\in\gamma(\alpha\beta)}[K_1^\gamma S_i^\gamma S_j^\gamma+\Gamma_1^\gamma(S_i^\alpha S_j^\beta+S_i^\beta S_j^\alpha)] \quad (7)$$

The symbols are the same as that in Eq. (6). In the $P3$ case, the symmetry allows $K_1^z=K_1^x=K_1^y$ and $\Gamma_1^z=\Gamma_1^x=\Gamma_1^y$, while in the $C2$ case $K_1^x=K_1^y=K_1^z+\delta_1$ and $\Gamma_1^x=\Gamma_1^y=\Gamma_1^z+\delta_2$ with a small amount δ_1 and δ_2.

B. Spin wave excitation

We now turn to the calculation of the spin wave excitations. To compare to the inelastic neutron scattering experiments, we use the SU(N)[36,37] spin wave theory to calculate the correlation function $\tilde{S}(\boldsymbol{q},\omega)$(zero temperature), which is defined as

$$\tilde{S}(\boldsymbol{q},\omega)=\frac{1}{N}\sum_{ij}e^{\mathrm{i}\boldsymbol{q}(\boldsymbol{r}_i-\boldsymbol{r}_j)}\int_{-\infty}^{\infty}\langle\boldsymbol{Q}_i\boldsymbol{Q}_j(t)\rangle\, e^{-\mathrm{i}\omega t}dt, \quad (8)$$

with $\boldsymbol{Q}_j(t)=e^{\mathrm{i}Ht}\boldsymbol{Q}e^{-\mathrm{i}Ht}$. Generally, $\boldsymbol{Q}=2\boldsymbol{s}_j+\boldsymbol{L}_j$ with $\boldsymbol{s}$ and $\boldsymbol{L}$ the spin and orbital angular momenta, respectively.

Firstly, to obtain the suitable values of K_1 and Γ_1 in the minimal isospin model of Eq. (7) for α-$RuCl_3$, we optimize K_1 and Γ_1 to make the low-energy isospin excitations of the model of Eq. (7) to be in accordance with those of the effective exchange model of Eq. (6) obtained through projecting the five-orbital Hubbard model to the Kramers doublet. The hopping parameters in the five-orbital Hubbard model are from the first-principle calculations, and the interaction parameters are chosen as $U=2.31$ eV, $J_H=0.32$ eV and $\lambda=0.14$ eV, which are appropriate for α-$RuCl_3$[15,19,29,32,35]. We find that $K_1^\gamma=-5.5$ meV and $\Gamma_1^\gamma=7.6$ meV ($K_1^z=-10.9$ meV, $K_1^x=-10.9$ meV, $\Gamma_1^z=6.2$ meV and $\Gamma_1^x=6.0$ meV) can give the results fitting well to those obtained by Eq. (6) in the $P3$ ($C2$) case as shown in Fig. 3. Moreover, for these parameters, the classical ground states of both the minimal isospin model of Eq. (7) and the effective exchange model of Eq. (6) show the same zigzag magnetic order.

We then perform the calculations of the SU(2) spin wave theory based on the minimal isospin model to compute the correlation function of Eq. (8) for the $J_{\rm eff}=1/2$ isospin. The results are presented in Fig. 3. We find that the isospin excitations show a gap at the M point and the maximal intensity is also near the M point, which agree well with the INS experiments[15,26,28]. Moreover, the direction of magnetic moment $\boldsymbol{m}$, which is the expectation value of total angular moment $\boldsymbol{J}=\boldsymbol{s}+\boldsymbol{L}$ with respect to the classical ground state, tilts 36° (48°) out of the ab plane in $P3$ ($C2$) case, which roughly coincides with the experimental result of Ref. 25.

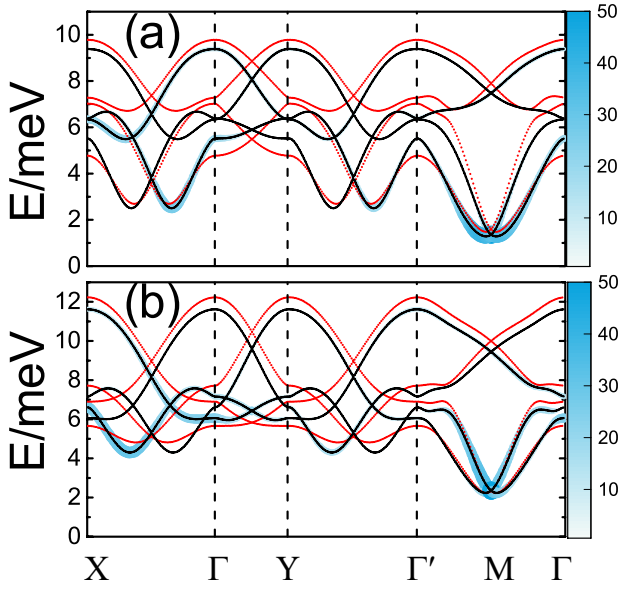

FIG. 3. (Color online) Spin wave dispersions along the high symmetry direction $X-\Gamma-Y-\Gamma'-M-\Gamma$ (see Fig. 1(b)) in (a) $P3$ case and (b) $C2$ case. The black solid and red dash lines correspond to the results calculated based on the minimal isospin model Eq.(7) and the effective isospin model Eq.(6) respectively. The size of colors indicate the magnitude of the isospin correlation function $\tilde{S}$ calculated based on the minimal isospin model Eq.(7).

As shown in Fig.3 (a) and (b), we can find the dispersions show no qualitative difference in the $P3$ and $C2$ cases, though the maximum intensities of $\tilde{S}$ near the M point in the two cases are in different branches. In addition, the gaps of the isospin excitations in the $P3$ and $C2$ cases are also consistent with each other, though the values of K_1 and Γ_1 are obviously different. If we artificially change the ratio of K_1 and Γ_1 to $|K_1|/|\Gamma_1|\approx 1.26$, the gap of the isospin excitations will closed.

To further check the validity of the $K-\Gamma$ model shown in Eq. (6), we then construct a more complex effective exchange model by projecting the five-orbital Hubbard model of Eq. (1) to the subspace of the lowest six many-body states of the $4d^5$ electron configuration, which includes both the $J_{\rm eff}=1/2$ doublet and the $J_{\rm eff}=3/2$ quartet, and study the isospin excitations in this effective model by the SU(N) spin-wave theory. The local operators of the effective Hamiltonian are now a 6×6 matrices on each site, so in the SU(N) spin-wave theory we express the effective Hamiltonian as a linear combination

of the generators of SU(6) and map these generators into the bosonic language. By performing the calculations of the SU(6) spin-wave theory, we find the ground state of this effective model is of a zigzag spin order, in which the Kramers doublet has the dominant weight. This result is a further support to the $J_{\rm eff} = 1/2$ isospin picture on which the minimal isospin model is based. More importantly, the low-energy spin-wave excitations (see Fig. 4) calculated from the SU(6) spin-wave theory based on this effective exchange model are consistent well with those of the minimal isospin model (Fig. 3). Thus, the minimal isospin exchange model derived in the last subsection is suitable for describing the low-energy physics in α-$RuCl_3$, and it can be used to other magnetic properties such as the physics of Kitaev spin liquid. In addition, besides the $J_{\rm eff} = 1/2$ isospin excitations, we expect that the spin-orbital excitations between the $J_{\rm eff} = 1/2$ and $J_{\rm eff} = 3/2$ states revealed by the SU(6) spin-wave calculations in the high-energy parts of Fig. 4 can be observed by the future resonant inelastic X-ray scattering (RIXS) experiments.

III. PARTICLE-HOLE EXCITATION AND PAIRING SYMMETRY IN DOPED SYSTEMS

In this section, we study various PH excitations and the possible superconductivity mediated by the PH excitations in doped systems. As the angle-resolved photoemission measurements reveal that the parent and electron-doped compounds of α-$RuCl_3$ are insulators[38], we here only study the hole-doping case. According to the above discussion, the low-energy physics of α-$RuCl_3$ is dominated by the t_{2g} orbitals, so we use a t_{2g} three-orbital model to simplify the calculations in this section. The three-orbital Hamiltonian is given by

$$H = H_{t_{2g}} + H_{int}, \tag{9}$$

where the parameters in the three-orbital tight-binding Hamiltonian $H_{t_{2g}}$ by fitting the DFT low-energy band structures are listed in Appendix A and H_{int} is the same as that in Eq.(4).

In order to include the SOC, we use the Hugenholtz diagrams to calculate the PH excitations in the RPA approach[39]. In this method, the susceptibilities from the PH excitations are given as

$$\widehat{\chi}(q) = \widehat{\chi}^0(q)\left[\widehat{1} + \widehat{\Gamma}\widehat{\chi}^0(q)\right]^{-1}, \tag{10}$$

where $\widehat{\Gamma}$ is the Hugenholtz bare vertex[39] and $\widehat{1}$ is the identity matrix. The non-interacting susceptibility is given by

$$\chi^0_{ij,\mu\nu}(q) = -\frac{T}{N}\sum_k G^0_{i\mu}(k+q)G^0_{\nu j}(k) \tag{11}$$

with the number of unit cell N and the temperature T. The bare Green's function is written as

$$\widehat{G}^0(k) = [\mathrm{i}\omega_n - \widehat{H}_{t_{2g}}(\boldsymbol{k}) + \mu]^{-1}. \tag{12}$$

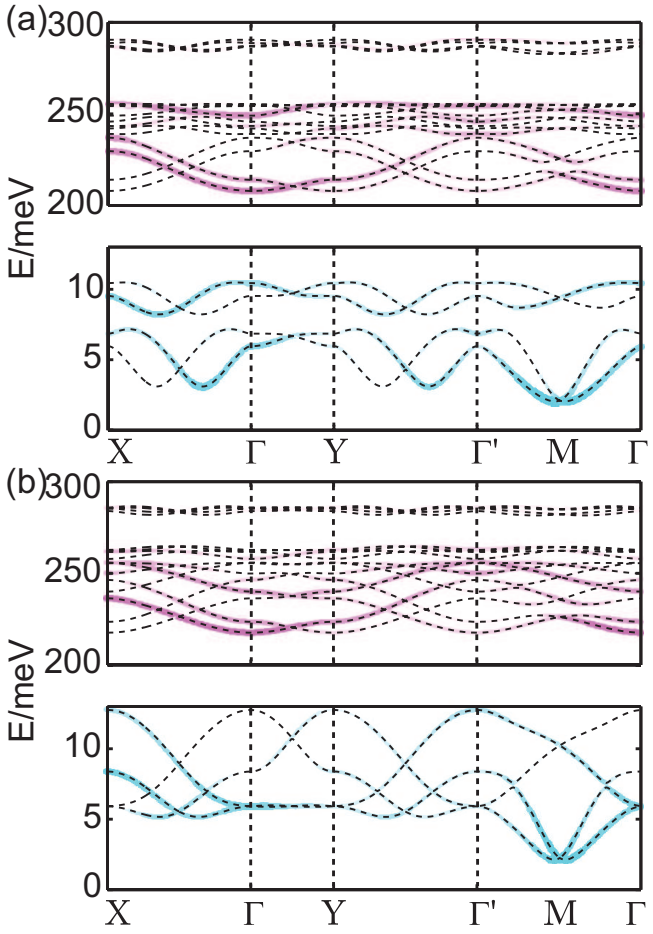

FIG. 4. (Color online) Spin wave dispersion (dashed) for the complex effective exchange model in (a) and (b) corresponding to $P3$ case and $C2$ case respectively. Cyan and magenta colors depict the magnitude of the isospin excitations and the spin-orbit excitations, respectively. The size of colors indicate the magnitude of $\tilde{S}$. A large gap between 200 meV and 13 meV results from SOC.

Here, the labels i, j, μ and ν involve all of the degrees of freedom (sublattice, orbital and spin) in an unit cell. Thus, for the three-orbital model on the honeycomb lattice, $\widehat{G}$ is a 12×12 matrix, while $\widehat{\chi}$, $\widehat{\chi}^0$ and $\widehat{\Gamma}$ are 144×144 matrices. In the above, $k \equiv [\boldsymbol{k}, \mathrm{i}\omega_n]$ ($q \equiv [\boldsymbol{q}, \mathrm{i}\omega_m]$) with $\omega_n = (2n+1)\pi T$ ($\omega_m = 2m\pi T$) for fermions (bosons).

Based on the scenario that the pairing interaction arises from the exchange of various PH excitations, the effective interaction in the particle-particle channel is given by[39]

$$\Gamma^{\rm eff}_{ij,\alpha\beta}(q) = [\frac{1}{2}\widehat{\Gamma} - \widehat{\Gamma}\widehat{\chi}(q)\widehat{\Gamma}]_{i\alpha,\beta j}. \tag{13}$$

The linearized superconducting gap equation is given by

$$-\frac{T}{N}\sum_{q,\alpha\beta\mu\nu}\Gamma^{\rm eff}_{ij,\alpha\beta}(q)G_{\alpha\mu}(k-q)G_{\beta\nu}(q-k) \times \Delta_{\mu\nu}(k-q) = \Lambda\Delta_{ij}(k). \tag{14}$$

Considering that the dominant scatterings occur near the Fermi surface (FS), we can project the effective pairing interaction Eq. (13) and the gap equation Eq. (14) on the FS. In this way, the scattering amplitude of a Cooper pair from the state $(\boldsymbol{k}, -\boldsymbol{k})$ on the γ_1 FS to the state $(\boldsymbol{k}', -\boldsymbol{k}')$ on the γ_2 FS is calculated by[40,41]

$$V_{\gamma_1\gamma_2}(\boldsymbol{k},\boldsymbol{k}') = \sum_{ij\alpha\beta} \psi^{i*}_{\gamma_1}(\boldsymbol{k})\psi^{j*}_{\gamma_1}(-\boldsymbol{k})\Gamma^{\text{eff}}_{ij,mn}(\boldsymbol{k}-\boldsymbol{k}',0) \times \psi^{\alpha}_{\gamma_2}(\boldsymbol{k}')\psi^{\beta}_{\gamma_2}(-\boldsymbol{k}'), \tag{15}$$

where $\psi^i_{\gamma_1}(\boldsymbol{k})$ is the γ_1th eigenvector of the $\widehat{H}_{t_{2g}}(\boldsymbol{k})$ matrix. Then we solve the following linearized gap equation,

$$-\sum_{\gamma_2}\oint_{FS}\frac{d\boldsymbol{k}'_{\parallel}}{4\pi^2 v^F_{\gamma_2}(\boldsymbol{k}')}V_{\gamma_1\gamma_2}(\boldsymbol{k},\boldsymbol{k}')\Delta_{\gamma_2}(\boldsymbol{k}') = \Lambda\Delta_{\gamma_1}(\boldsymbol{k}), \tag{16}$$

where $v^F_{\gamma_2}(\boldsymbol{k}')$ is the Fermi velocity for the band γ_2 and $\Delta_{\gamma_1}(\boldsymbol{k})$ represents the normalized gap function along the FS γ_1. The integration and summation in Eq. (16) are along various FS patches. Here, the temperature is set at $T = 0.001$eV and the calculation of the susceptibility is done with uniform 64×64 meshes in the momentum space. This equation can be solved as an eigenvalue problem, where the largest eigenvalue Λ determines the favourable pairing symmetry.

Let us first study the main properties of the PH excitations in the doped system. In order to find out the dominant PH excitations, we classify various PH channels according to the total angular momentum J of a PH pair. Generally, the susceptibility can be written in terms of $\widehat{F}_{\alpha\beta} = d^\dagger_\alpha d_\beta$, i.e. $\chi_{\mu\nu,\alpha\beta} = \left\langle \widehat{F}_{\nu\mu}\widehat{F}_{\alpha\beta}\right\rangle$. To show the labels of the effective angular momentums explicitly, we can express the annihilation operator of electrons as $d_{\zeta jm}$, where j and m indicate the total effective angular momentum and its z component respectively, ζ contains other quantum numbers except the angular momentum. Then, the PH excitation operators are written as $\widehat{F}^{\zeta_1\zeta_2}_{j_1m_1,j_2m_2} = d^\dagger_{\zeta_1 j_1 m_1} d_{\zeta_2 j_2 m_2}$, which are tensor operators. Since the representation of $d^\dagger_{\zeta jm}$ and $d_{\zeta jm}$ are $D^{\frac{1}{2}}\oplus D^{\frac{3}{2}}$ in the sector of effective angular momentum, the operator $\widehat{F}^{\zeta_1\zeta_2}_{j_1m_1,j_2m_2}$ has the following decomposition in the sector of effective angular momentum,

$$\begin{aligned}\widehat{F}^{\zeta_1\zeta_2}_{j_1m_1,j_2m_2} &\in (D^{\frac{1}{2}}\oplus D^{\frac{3}{2}})\otimes(D^{\frac{1}{2}}\oplus D^{\frac{3}{2}}) \\ &= 2D^0\oplus 4D^1\oplus 3D^2\oplus D^3.\end{aligned} \tag{17}$$

Thus, the operator $\widehat{F}$ could be divided into irreducible tensor operators $\widehat{T}^{j_1j_2}_{jm}(\zeta_1\zeta_2)$ as given in Appendix B. Here, j_1 and j_2 are the quantum number of the particle and hole, j and m are the quantum number for the total angular momentum and its z component of the PH pair. Therefore, including the sublattice indices on the honeycomb lattice, the susceptibilities χ are split into 144×144 channels which include $J_{\text{eff}} = 1/2$ excitations,

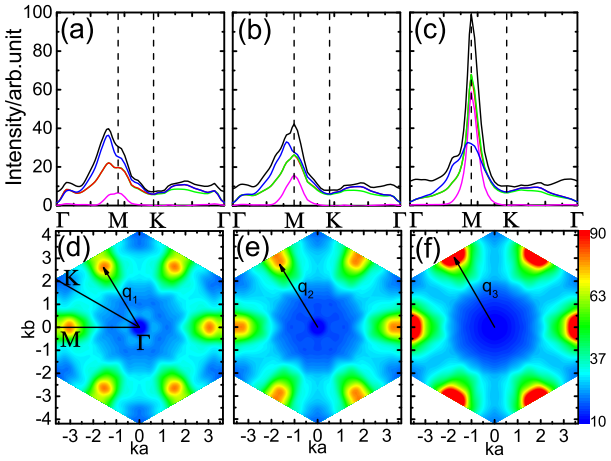

FIG. 5. (Color online) Static susceptibilities for different electron concentrations: (a) and (d) $n_e = 9.8$, (b) and (e) $n_e = 9.7$, (c) and (f) $n_e = 9.6$. Up panels: the S^{zz} (blue), S^{xx} (green), S^{yy} (red),$-S^{xy}$ (magenta) and the largest eigenvalue of $\hat{\chi}^h$ (black) susceptibilities along the $\Gamma - M - K - \Gamma$ path. The solid lines are renormalized susceptibilities. Bottom panels: the distribution of $\sum_\eta S^{\eta\eta}(\boldsymbol{q})$ susceptibilities over the first Brillouin zone. The vectors indicate the positions of the peaks in susceptibilities.

$J_{\text{eff}} = 3/2$ excitations and various spin-orbit excitations between the $J_{\text{eff}} = 1/2$ and $J_{\text{eff}} = 3/2$ states. Among these channels, we find numerically that the $J_{\text{eff}} = 1/2$ isospin fluctuations $S^{\eta_1\eta_2}(\boldsymbol{q})$ are dominant. This implies that the scenario of $J_{\text{eff}} = 1/2$ isospin is also valid in the doped systems of α-$RuCl_3$. The $J_{\text{eff}} = 1/2$ isospin susceptibilities $S^{\eta_1\eta_2}(\boldsymbol{q})$ are defined as

$$S^{\eta_1\eta_2}(\boldsymbol{q}) = \frac{T}{2N}\sum_{\ell_1\ell_2}\int_0^{\frac{1}{T}}\langle T_\tau S^{\eta_1}_{\ell_1}(\boldsymbol{q},\tau)S^{\eta_2}_{\ell_2}(-\boldsymbol{q},0)\rangle d\tau, \tag{18}$$

where ℓ_1 and ℓ_2 are the sublattice indices, and the isospin operators S^η_ℓ are given by

$$\begin{aligned} S^x_\ell &= \frac{1}{\sqrt{2}}(-\widehat{T}^{\frac{1}{2}\frac{1}{2}}_{1,1}(\ell\ell) + \widehat{T}^{\frac{1}{2}\frac{1}{2}}_{1,-1}(\ell\ell)), \\ S^y_\ell &= \frac{\mathrm{i}}{\sqrt{2}}(\widehat{T}^{\frac{1}{2}\frac{1}{2}}_{1,1}(\ell\ell) + \widehat{T}^{\frac{1}{2}\frac{1}{2}}_{1,-1}(\ell\ell)), \\ S^z_\ell &= \widehat{T}^{\frac{1}{2}\frac{1}{2}}_{1,0}(\ell\ell). \end{aligned} \tag{19}$$

When interactions are increased, the magnitude of isospin fluctuations are drastically enhanced in contrast to other types of fluctuations.

In Fig. 5(a)-(c), we show the diagonal (S^{xx}, S^{yy}, S^{zz}) and off-diagonal (S^{xy}) channels of the isospin susceptibilities together with the largest eigenvalue of $\hat{\chi}$ along the $\Gamma - M - K - \Gamma$ path (see Fig. 5(d)) for the number of electrons in primitive cell $n_e = 9.8, 9.7$ and 9.6 (in the parent compound, $n_e = 10$). It can be seen that the isospin susceptibilities capture the main features of the maximal eigenvalue of $\hat{\chi}$. The differences of S^{xx}, S^{yy} and S^{zz} shown in Fig. 5(a)-(c) are the reflections

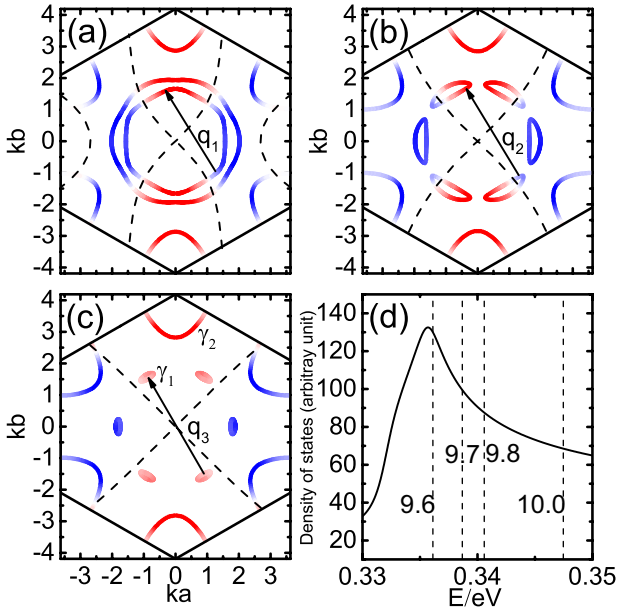

FIG. 6. (Color online) Dominant gap functions $\Delta(\boldsymbol{k})$ and their sign structures along the FSs for different hole doping. (a) $n_e = 9.8$, (b) $n_e = 9.7$, (c) $n_e = 9.6$. The signs of gap functions are shown by the following colors: red (positive) and blue (negative). The lines with an arrow indicate the nesting vectors related to the peaks of the isospin fluctuations. Dashed lines denotes the fit gaps (see text). γ_1 and γ_2 label the FSs. (d) The dash lines from right to left correspond to $n_e = 10, 9.8, 9.7, 9.6$ respectively.

of the asymmetry of the Kitaev exchange interaction in the weak-coupling limit. Especially, when rotating 120 degrees clockwise along k_c-axis, the transformation of isospin fluctuations has a cycle rule: $(x, y, z) \to (y, z, x)$, namely $S^{xx} \to S^{yy}, S^{yy} \to S^{zz}$ and $S^{zz} \to S^{xx}$. For $n_e = 9.8$ (Fig. 5(a)), the peaks of the susceptibilities deviate from the M point. When the electron concentration is decreased, the peaks move to M point, meanwhile the intensities of the peaks are enhanced except for S^{zz} and show a divergent tendency (see Fig. 5(c)). To be more clear, we present the contour plots of $\sum_\eta S^{\eta\eta}(\boldsymbol{q})$ in Fig. 5(d)-(f) where the peaks are labeled by $\boldsymbol{q_1}, \boldsymbol{q_2}$ and $\boldsymbol{q_3}$ respectively. The peaks of the susceptibilities are related to the nesting property of the FS as shown by the vectors $\boldsymbol{q_1}, \boldsymbol{q_2}$ and $\boldsymbol{q_3}$ in Fig. 6. The divergence of the susceptibilities means that the system has an SDW instability around $n = 9.6$. The origin of this SDW is that the Fermi level is close to the point of van Hove singularity (see Fig. 6(d)) which results the divergence of the density of states and thus enhances the particle-hole excitations. We note that the peaks of the susceptibilities are located at M point, so this SDW state also exhibits a zigzag magnetic order.

We then study the properties of superconducting pairing by solving Eq. (16). We find that the maximal values of Λ are in the pseudospin-singlet pairing channel and are far greater than those of the pseudospin-triplet pairing modes. The leading pairing functions are consistent with the $d_{x^2+y^2} + \mathrm{i}d_{xy}$ wave, which belongs to a two dimensional irreducible representation of the D_{3d} group. In Fig. 6(a)-(c), we present the real parts of the leading pairing functions for three different electron concentrations. To understanding the detailed forms of the pairing functions, we fit the gap functions by including the electron pairings up to the third NN pairing in the real space. The fitting functions are given by

$$\Delta_n(\boldsymbol{k}) = \Delta_1 d^{(1)}_{x^2-y^2}(\boldsymbol{k}) + \Delta_2 d^{(2)}_{x^2-y^2}(\boldsymbol{k}) + \Delta_3 d^{(3)}_{x^2-y^2}(\boldsymbol{k}), \tag{20}$$

where $d^{(1)}_{x^2-y^2}(\boldsymbol{k}) = \cos(\frac{ka}{\sqrt{3}}) - \cos(\frac{ka}{2\sqrt{3}})\cos(\frac{kb}{2})$, $\Delta_2 d^{(2)}_{x^2-y^2}(\boldsymbol{k}) = \cos(kb) - \cos(\frac{\sqrt{3}}{2}ka)\cos(\frac{kb}{2})$ and $\Delta_3 d^{(3)}_{x^2-y^2}(\boldsymbol{k}) = \cos(\frac{2ka}{\sqrt{3}}) - \cos(\frac{ka}{\sqrt{3}})\cos(kb)$ are for the first, second and third NN pairings respectively, and Δ_1, Δ_2 and Δ_3 are the corresponding pairing intensities. Here, n denotes the electron concentration. Through adjusting the values of Δ_1, Δ_2 and Δ_3, we find the following optimal fitting functions for the three electron concentrations,

$$\begin{aligned}
\Delta_{9.8}(\boldsymbol{k}) &= 0.11 d^{(1)}_{x^2-y^2}(\boldsymbol{k}) + 0.55 d^{(2)}_{x^2-y^2}(\boldsymbol{k}) \\
&\quad + 0.83 d^{(3)}_{x^2-y^2}(\boldsymbol{k}), \\
\Delta_{9.7}(\boldsymbol{k}) &= 0.96 d^{(1)}_{x^2-y^2}(\boldsymbol{k}) + 0.07 d^{(2)}_{x^2-y^2}(\boldsymbol{k}) \\
&\quad + 0.26 d^{(3)}_{x^2-y^2}(\boldsymbol{k}), \\
\Delta_{9.6}(\boldsymbol{k}) &= 0.80 d^{(1)}_{x^2-y^2}(\boldsymbol{k}) - 0.56 d^{(2)}_{x^2-y^2}(\boldsymbol{k}) \\
&\quad + 0.22 d^{(3)}_{x^2-y^2}(\boldsymbol{k}).
\end{aligned} \tag{21}$$

To be more clear, we depict the nodal lines of the gap functions in Fig. 6(a)-(c) by the dashed lines.

IV. SUMMARY

In summary, we derive a minimal effective isospin model from the five-orbital Hubbard model using the energy bands obtained from the first-principle calculations for α-$RuCl_3$. The minimal model contains the ferromagnetic Kitaev term and the antiferromagnetic off-diagonal exchange term. Based on this model, we investigate the spin-wave excitation using the linear spin wave theory and find it is consistent with the recent neutron scattering on α-$RuCl_3$. We also investigate various particle-hole excitations and possible superconducting pairing symmetry in the doped systems by use of the random-phase approximation. Our results show that the $J_{\text{eff}} = 1/2$ picture is robust in the doped systems, and the d-wave pairing is the most favourable superconducting pairing symmetry.

ACKNOWLEDGMENTS

This work was supported by the National Natural Science Foundation of China (11190023, 11374138 and 11674158) and National Key Projects for Research and Development of China (Grant No. 2016YFA0300401).

Appendix A: tight bind model

The electronic structure calculations were performed with the generalized gradient approximation for the exchange-correlation functional as implemented in Quantum ESPRESSO package[42] based on density-functional theory (DFT). To avoid taking SOC into account double[29], the SOC were not included in these calculations. Firstly, the five-orbital hopping parameters (TB5) from maximally-localized Wannier orbital[43] calculation are shown in Table I and Table II. Table I (Table II) exhibits the hopping matrix $\mathcal{T}_{ij}$, where $H_t = \sum_{ij,\sigma} \psi^\dagger_{i,\sigma} \mathcal{T}_{ij} \psi_{j,\sigma}$, of some bonds. For other bonds in $P3$ ($C2$) case, the hopping matrix can be recovered by applying inversion operations and C_3 rotations along the c-axis perpendicular to the ab plane (C_2 rotations along the Z_1-bond). The orbital angular momenta acting on d orbital space are expressed by

$$L^x = \begin{pmatrix} 0 & 0 & \mathrm{i}\sqrt{3} & 0 & 0 \\ 0 & 0 & \mathrm{i} & 0 & 0 \\ -\mathrm{i}\sqrt{3} & -\mathrm{i} & 0 & 0 & 0 \\ 0 & 0 & 0 & 0 & \mathrm{i} \\ 0 & 0 & 0 & -\mathrm{i} & 0 \end{pmatrix},$$

$$L^y = \begin{pmatrix} 0 & 0 & 0 & -\mathrm{i}\sqrt{3} & 0 \\ 0 & 0 & 0 & \mathrm{i} & 0 \\ 0 & 0 & 0 & 0 & -\mathrm{i} \\ \mathrm{i}\sqrt{3} & -\mathrm{i} & 0 & 0 & 0 \\ 0 & 0 & \mathrm{i} & 0 & 0 \end{pmatrix},$$

$$L^z = \begin{pmatrix} 0 & 0 & 0 & 0 & 0 \\ 0 & 0 & 0 & 0 & -2\mathrm{i} \\ 0 & 0 & 0 & \mathrm{i} & 0 \\ 0 & 0 & -\mathrm{i} & 0 & 0 \\ 0 & 2\mathrm{i} & 0 & 0 & 0 \end{pmatrix}.$$

The three-orbital tight bind Hamiltonian (TB3) is $H_{t_{2g}} = \sum_{ij} \psi'^\dagger_i \mathcal{T}'_{ij} \psi'_j + \lambda \sum_i \boldsymbol{s}_i \cdot \boldsymbol{L}'_i$, where $\mathcal{T}'_{ij}$ are given in Table.III and $\boldsymbol{L}'_i$ is found by projecting $\boldsymbol{L}_i$ into t_{2g} states. The crystal field in $P3$ case is given by

$$h^{\Delta}_{i,\sigma} = \begin{pmatrix} \Delta & 0 & \Delta_2 & \Delta_2 & -2\Delta_2 \\ 0 & \Delta & -\sqrt{3}\Delta_2 & \sqrt{3}\Delta_2 & 0 \\ \Delta_2 & -\sqrt{3}\Delta_2 & 0 & \Delta_3 & \Delta_3 \\ \Delta_2 & \sqrt{3}\Delta_2 & \Delta_3 & 0 & \Delta_3 \\ -2\Delta_2 & 0 & \Delta_3 & \Delta_3 & 0 \end{pmatrix} \quad \text{(A1)}$$

TABLE I. Hopping parameters for five-orbital model in $P3$ case (meV). A and B are sublattice indices, Z_1, Z_2 and Z_3 bonds are expressed in Fig. 1(a).

Bond		$\mathcal{T}_{ij}$				
		d_{z^2}	$d_{x^2-y^2}$	d_{yz}	d_{xz}	d_{xy}
Z_1:	d_{z^2}	23.0	0.0	-0.7	-0.7	212.4
$A \to B$	$d_{x^2-y^2}$	0.0	-91.0	-0.3	0.3	0.0
	d_{yz}	-0.7	-0.3	61.4	108.7	-4.5
	d_{xz}	-0.7	0.3	108.7	61.4	-4.5
	d_{xy}	212.4	0.0	-4.5	-4.5	-206.9
Z_2:	d_{z^2}	4.6	-1.5	-15.9	-8.4	65.9
$A \to A$	$d_{x^2-y^2}$	1.8	-2.2	-1.3	3.5	2.1
	d_{yz}	-8.3	-3.6	-0.3	-37.0	4.6
	d_{xz}	-15.8	1.0	-58.0	-0.3	6.3
	d_{xy}	65.8	-2.1	6.3	4.6	-0.5
Z_3:	d_{z^2}	-30.6	0.0	-6.1	-6.1	26.0
$A \to B$	$d_{x^2-y^2}$	0.0	72.8	5.7	-5.7	0.0
	d_{yz}	-6.1	5.7	6.4	-7.5	9.0
	d_{xz}	-6.1	-5.7	-7.5	6.4	9.0
	d_{xy}	26.0	0.0	9.0	9.0	-44.2

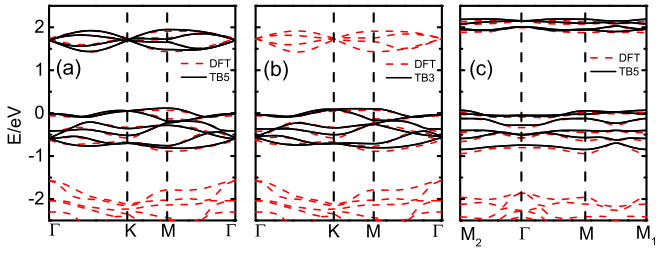

FIG. 7. (Color online) Band structure of α-$RuCl_3$ monolayer. The dashed red lines show the result from DFT without SOC, and tight bind bands from (a) five-orbital model of $P3$ case (b) three-orbital model of $P3$ case (c) five-orbital model of $C2$ case are in black solid lines. For $C2$ case, high symmetry points M_1 and M_2 are mid-points of reciprocal lattice vectors.

with $\Delta = 1980$ meV, $\Delta_2 = 15$ meV and $\Delta_3 = -8.6$ meV. And in $C2$ case the crystal field is written as follows

$$h^{\Delta}_{i,\sigma} = \begin{pmatrix} \Delta + 4.4 & 0 & 8.1 & 8.1 & -64.2 \\ 0 & \Delta & -60.9 & 60.9 & 0 \\ 8.1 & -60.9 & 0 & -8.1 & -7.0 \\ 8.1 & 60.9 & -8.1 & 0 & -7.0 \\ -64.2 & 0 & -7.0 & -7.0 & -3.4 \end{pmatrix} \quad \text{(A2)}$$

with $\Delta = 2272.5$ meV. The comparison of the DFT computed band structure and the tight bind fits including TB5 and TB3 without SOC are shown in Fig. 7.

TABLE II. Hopping parameters for five-orbital model in $C2$ case (meV). A and B are sublattice indices, $Z_{1,2,3}$ and $X_{1,2,3}$ bonds are expressed in Fig. 1(a).

Bond		$\mathcal{T}_{ij}$				
		d_{z^2}	$d_{x^2-y^2}$	d_{yz}	d_{xz}	d_{xy}
Z_1:	d_{z^2}	22.9	0.0	13.8	13.8	268.0
$A \to B$	$d_{x^2-y^2}$	0.0	-30.4	-7.5	7.5	0.0
	d_{yz}	13.8	-7.5	42.8	156.6	-21.4
	d_{xz}	13.8	7.5	156.6	42.8	-21.4
	d_{xy}	268.0	0.0	-21.4	-21.4	-117.1
X_1:	d_{z^2}	-14.9	-16.8	-137.3	2.3	-9.8
$A \to B$	$d_{x^2-y^2}$	-16.8	11.4	232.7	11.7	2.8
	d_{yz}	-137.3	232.7	-104.5	-12.7	-13.2
	d_{xz}	2.3	11.7	-12.7	42.1	159.9
	d_{xy}	-9.8	2.8	-13.2	159.9	41.6
Z_2:	d_{z^2}	12.2	-5.7	-15.5	-11.8	73.0
$A \to A$	$d_{x^2-y^2}$	5.7	-1.1	-2.7	4.6	4.2
	d_{yz}	-11.8	-4.6	-5.9	-43.5	-0.9
	d_{xz}	-15.5	2.7	-63.1	-5.9	8.5
	d_{xy}	73.0	-4.2	8.5	-0.9	-4.6
X_2:	d_{z^2}	1.9	0.2	-33.1	9.6	3.9
$A \to A$	$d_{x^2-y^2}$	-11.5	9.9	65.3	-7.4	-13.7
	d_{yz}	-40.2	61.3	-4.3	-0.5	8.8
	d_{xz}	9.9	-11.3	10.5	-6.7	-63.2
	d_{xy}	1.4	-13.0	0.4	-44.0	-5.5
Z_3:	d_{z^2}	-26.1	0.0	-6.8	-6.8	22.5
$A \to B$	$d_{x^2-y^2}$	0.0	56.9	4.7	-4.7	0.0
	d_{yz}	-6.8	4.7	6.6	-10.6	12.4
	d_{xz}	-6.8	-4.7	-10.6	6.6	12.4
	d_{xy}	22.5	0.0	12.4	12.4	-39.9
X_3:	d_{z^2}	35.3	35.1	-12.4	-0.5	7.7
$A \to B$	$d_{x^2-y^2}$	35.1	-5.1	18.3	-8.6	-3.4
	d_{yz}	-12.4	18.3	-39.9	13.1	12.3
	d_{xz}	-0.5	-8.6	13.1	6.3	-10.6
	d_{xy}	7.7	-3.4	12.3	-10.6	6.4

TABLE III. Hopping parameters for three-orbital model in $P3$ case (meV). A and B are sublattice indices, Z_1, Z_2 and Z_3 bonds are expressed in Fig. 1(a).

Bond		$\mathcal{T}'_{ij}$		
		d_{yz}	d_{xz}	d_{xy}
Z_1:	d_{yz}	58.7	113.9	-7.0
$A \to B$	d_{xz}	113.9	58.7	-7.0
	d_{xy}	-7.0	-7.0	-194.1
Z_2:	d_{yz}	-0.7	-27.6	3.6
$A \to A$	d_{xz}	-51.9	-0.7	6.2
	d_{xy}	6.2	3.6	1.6
Z_3:	d_{yz}	-6.3	-4.8	10.7
$A \to B$	d_{xx}	-4.8	-6.3	10.7
	d_{xy}	10.7	10.7	-43.9

Appendix B: particle-hole channels

The PH operators $\widehat{F}^{\zeta_1\zeta_2}_{j_1m_1,j_2m_2} = d^\dagger_{\zeta_1 j_1 m_1} d_{\zeta_2 j_2 m_2}$ under rotations have the following properties,

$$\begin{aligned}\widehat{F}^{\zeta_1\zeta_2}_{j_1m_1,j_2m_2} &\to \sum_{m'_1m'_2} \widehat{F}^{\zeta_1\zeta_2}_{j_1m'_1,j_2m'_2} D^{j_1}_{m'_1,m_1}(R) D^{j_2*}_{m'_2,m_2}(R) \\ &= \sum_{m'_1m'_2} \widehat{F}^{\zeta_1\zeta_2}_{j_1m'_1,j_2m'_2} D^{j_1}_{m'_1,m_1}(R) D^{j_2}_{-m'_2,-m_2}(R) \\ &\quad \times (-1)^{2j_2-m_2-m'_2} \\ &= \sum_{jmm'm'_1m'_2} \widehat{F}^{\zeta_1\zeta_2}_{j_1m'_1,j_2m'_2} C^{j_1j_2j}_{m'_1-m'_2m} C^{j_1j_2j}_{m_1-m_2m'} \\ &\quad \times D^{j}_{m,m'}(R)(-1)^{2j_2-m_2-m'_2}.\end{aligned} \tag{B1}$$

Here, $C^{j_1j_2j}_{m_1-m_2m'}$ are the Clebsch-Gordan coefficients and $D^{j_1}_{m'_1,m_1}(R)$ is the representation of the group element R in SU(2). Thus, an irreducible representation of SU(2) is written as

$$\begin{aligned}\widehat{T}^{j_1j_2}_{jm}(\zeta_1\zeta_2) = &\sum_{m_1m_2} d^\dagger_{\zeta_1 j_1 m_1} d_{\zeta_2 j_2 m_2} C^{j_1j_2j}_{m_1-m_2m} \\ &\times (-1)^{j_2-m_2} N(jm),\end{aligned} \tag{B2}$$

where $N(jm)$ is a normalized factor. The tensor operators satisfy the relation $\widehat{T}^{\dagger j_1 j_2}_{jm}(\zeta_1\zeta_2) = \widehat{T}^{j_2j_1}_{j-m}(\zeta_2\zeta_1)(-1)^{j_2-j_1+m}$. For example, the explicit formalism of $\widehat{T}^{j_1=\frac{1}{2}j_2=j_1}_{j=1,0m}(\ell_1\ell_2)$ are given by

$$\begin{aligned}\widehat{T}^{\frac{1}{2}\frac{1}{2}}_{00}(\ell_1\ell_2) =& \frac{1}{\sqrt{2}}(d^\dagger_{\ell_1\frac{1}{2}\frac{1}{2}} d_{\ell_2\frac{1}{2}\frac{1}{2}} + d^\dagger_{\ell_1\frac{1}{2}\frac{-1}{2}} d_{\ell_2\frac{1}{2}\frac{-1}{2}}), \\ \widehat{T}^{\frac{1}{2}\frac{1}{2}}_{10}(\ell_1\ell_2) =& \frac{1}{\sqrt{2}}(d^\dagger_{\ell_1\frac{1}{2}\frac{1}{2}} d_{\ell_2\frac{1}{2}\frac{1}{2}} - d^\dagger_{\ell_1\frac{1}{2}\frac{-1}{2}} d_{\ell_2\frac{1}{2}\frac{-1}{2}}) \\ \widehat{T}^{\frac{1}{2}\frac{1}{2}}_{11}(\ell_1\ell_2) =& - d^\dagger_{\ell_1\frac{1}{2}\frac{1}{2}} d_{\ell_2\frac{1}{2}\frac{-1}{2}}, \\ \widehat{T}^{\frac{1}{2}\frac{1}{2}}_{1-1}(\ell_1\ell_2) =& d^\dagger_{\ell_1\frac{1}{2}\frac{-1}{2}} d_{\ell_2\frac{1}{2}\frac{1}{2}}\end{aligned} \tag{B3}$$

Here, the operators $d_{i,jm}$ are set by a unitary transformation,

$$\begin{pmatrix} d_{i,\frac{1}{2}\frac{1}{2}} \\ d_{i,\frac{1}{2}\frac{-1}{2}} \\ d_{i,\frac{3}{2}\frac{3}{2}} \\ d_{i,\frac{3}{2}\frac{1}{2}} \\ d_{i,\frac{3}{2}\frac{-1}{2}} \\ d_{i,\frac{3}{2}\frac{-3}{2}} \end{pmatrix} = \begin{pmatrix} 0 & 0 & \frac{-1}{\sqrt{3}} & \frac{-1}{\sqrt{3}} & \frac{\mathrm{i}}{\sqrt{3}} & 0 \\ \frac{-1}{\sqrt{3}} & \frac{-\mathrm{i}}{\sqrt{3}} & 0 & 0 & 0 & \frac{1}{\sqrt{3}} \\ \frac{\mathrm{i}}{\sqrt{2}} & \frac{1}{\sqrt{2}} & 0 & 0 & 0 & 0 \\ 0 & 0 & \frac{-2\mathrm{i}}{\sqrt{6}} & \frac{\mathrm{i}}{\sqrt{6}} & \frac{1}{\sqrt{6}} & 0 \\ \frac{-\mathrm{i}}{\sqrt{6}} & \frac{1}{\sqrt{6}} & 0 & 0 & 0 & \frac{-2\mathrm{i}}{\sqrt{6}} \\ 0 & 0 & 0 & \frac{-\mathrm{i}}{\sqrt{2}} & \frac{1}{\sqrt{2}} & 0 \end{pmatrix} \begin{pmatrix} d_{i,yz\uparrow} \\ d_{i,xz\uparrow} \\ d_{i,xy\uparrow} \\ d_{i,yz\downarrow} \\ d_{i,xz\downarrow} \\ d_{i,xy\downarrow} \end{pmatrix} \tag{B4}$$

Then it is convenient to introduce the Hermitian operators defined as

$$S^{j_1j_2}_{jm,1}(\ell_1\ell_2) = \frac{1}{\sqrt{2}}(\widehat{T}^{j_1j_2}_{jm}(\ell_1\ell_2) + \widehat{T}^{\dagger j_1j_2}_{jm}(\ell_1\ell_2))$$
$$S^{j_1j_2}_{jm,2}(\ell_1\ell_2) = \frac{\mathrm{i}}{\sqrt{2}}(\widehat{T}^{j_1j_2}_{jm}(\ell_1\ell_2) - \widehat{T}^{\dagger j_1j_2}_{jm}(\ell_1\ell_2)) \quad \text{(B5)}$$

with $m < 0$ or $(m = 0, \ell_1 \neq \ell_2)$. For $m = 0$ and $\ell_1 = \ell_2$, the operator $S^{j_1j_2}_{jm,0} = \widehat{T}^{j_1j_2}_{jm}(\ell_1\ell_2)$ is real. Especially, under condition $j = 1$, $\ell_1 = \ell_2$ and $j_1 = j_2$, the Hermitian operators are spin operators such as $S^{\alpha}_{\ell_1}(\alpha = x, y, z)$. According these operators, the susceptibility $\widehat{\chi}^h(q)$ is divided into 144×144 channels which include AB sublattice fluctuations and the different angular momentum j fluctuations.

* jxli@nju.edu.cn

[1] J. Kim, D. Casa, M. H. Upton, T. Gog, Y.-J. Kim, J. F. Mitchell, M. van Veenendaal, M. Daghofer, J. van den Brink, G. Khaliullin, and B. J. Kim, Phys. Rev. Lett. **108**, 177003 (2012).

[2] J. Kim, M. Daghofer, a. H. Said, T. Gog, J. van den Brink, G. Khaliullin, and B. J. Kim, Nat. Commun. **5**, 4453 (2014).

[3] B. Kim, H. Jin, S. Moon, J.-Y. Kim, B.-G. Park, C. Leem, J. Yu, T. Noh, C. Kim, S.-J. Oh, J.-H. Park, V. Durairaj, G. Cao, and E. Rotenberg, Phys. Rev. Lett. **101**, 076402 (2008).

[4] A. Kitaev, Ann. Phys. (N. Y). **321**, 2 (2006).

[5] G. Jackeli and G. Khaliullin, Phys. Rev. Lett. **102**, 017205 (2009).

[6] S. K. Choi, R. Coldea, A. N. Kolmogorov, T. Lancaster, I. I. Mazin, S. J. Blundell, P. G. Radaelli, Y. Singh, P. Gegenwart, K. R. Choi, S.-W. Cheong, P. J. Baker, C. Stock, and J. Taylor, Phys. Rev. Lett. **108**, 127204 (2012).

[7] S. Hwan Chun, J. J.-W. Kim, J. J.-W. Kim, H. Zheng, C. C. Stoumpos, C. D. Malliakas, J. F. Mitchell, K. Mehlawat, Y. Singh, Y. Choi, T. Gog, A. Al-Zein, M. M. Sala, M. Krisch, J. Chaloupka, G. Jackeli, G. Khaliullin, and B. J. Kim, Nat. Phys. **11**, 462 (2015).

[8] H. Gretarsson, J. P. Clancy, X. Liu, J. P. Hill, E. Bozin, Y. Singh, S. Manni, P. Gegenwart, J. Kim, A. H. Said, D. Casa, T. Gog, M. H. Upton, H.-S. Kim, J. Yu, V. M. Katukuri, L. Hozoi, J. van den Brink, and Y.-J. Kim, Phys. Rev. Lett. **110**, 076402 (2013).

[9] H. Gretarsson, J. P. Clancy, Y. Singh, P. Gegenwart, J. P. Hill, J. Kim, M. H. Upton, A. H. Said, D. Casa, T. Gog, and Y.-J. Kim, Phys. Rev. B **87**, 220407 (2013).

[10] J. c. v. Chaloupka, G. Jackeli, and G. Khaliullin, Phys. Rev. Lett. **110**, 097204 (2013).

[11] Y. Singh, S. Manni, J. Reuther, T. Berlijn, R. Thomale, W. Ku, S. Trebst, and P. Gegenwart, Phys. Rev. Lett. **108**, 127203 (2012).

[12] J. c. v. Chaloupka, G. Jackeli, and G. Khaliullin, Phys. Rev. Lett. **105**, 027204 (2010).

[13] K. Foyevtsova, H. O. Jeschke, I. I. Mazin, D. I. Khomskii, and R. Valentí, Phys. Rev. B **88**, 035107 (2013).

[14] M. Majumder, M. Schmidt, H. Rosner, A. A. Tsirlin, H. Yasuoka, and M. Baenitz, Phys. Rev. B **91**, 180401 (2015).

[15] A. Banerjee, C. A. Bridges, J.-Q. Yan, A. A. Aczel, L. Li, M. B. Stone, G. E. Granroth, M. D. Lumsden, Y. Yiu, J. Knolle, S. Bhattacharjee, D. L. Kovrizhin, R. Moessner, D. A. Tennant, D. G. Mandrus, and S. E. Nagler, Nat. Mater. **15**, 733 (2016).

[16] R. D. Johnson, S. C. Williams, A. A. Haghighirad, J. Singleton, V. Zapf, P. Manuel, I. I. Mazin, Y. Li, H. O. Jeschke, R. Valentí, and R. Coldea, Phys. Rev. B **92**, 235119 (2015).

[17] K. W. Plumb, J. P. Clancy, L. J. Sandilands, V. V. Shankar, Y. F. Hu, K. S. Burch, H.-Y. Kee, and Y.-J. Kim, Phys. Rev. B **90**, 041112 (2014).

[18] B. H. Kim, T. Shirakawa, and S. Yunoki, arXiv:1606.06836.

[19] A. Koitzsch, C. Habenicht, E. Müller, M. Knupfer, B. Büchner, H. C. Kandpal, J. van den Brink, D. Nowak, A. Isaeva, and T. Doert, Phys. Rev. Lett. **117**, 126403 (2016).

[20] J. A. Sears, M. Songvilay, K. W. Plumb, J. P. Clancy, Y. Qiu, Y. Zhao, D. Parshall, and Y.-J. Kim, Phys. Rev. B **91**, 144420 (2015).

[21] E. V. Stroganov and K. V. Ovchinnikov, Ser. Fiz. i Khim. **12**, 152 (1957).

[22] Y. Kubota, H. Tanaka, T. Ono, Y. Narumi, and K. Kindo, Phys. Rev. B **91**, 094422 (2015).

[23] K. Brodersen, G. Thiele, H. Ohnsorge, I. Recke, and F. Moers, J. Less-Common Met. **15**, 347 (1968).

[24] J. M. Fletcher, W. E. Gardner, A. C. Fox, and G. Topping, J. Chem. Soc. A **0**, 1038 (1967).

[25] H. B. Cao, A. Banerjee, J.-Q. Yan, C. A. Bridges, M. D. Lumsden, D. G. Mandrus, D. A. Tennant, B. C. Chakoumakos, and S. E. Nagler, Phys. Rev. B **93**, 134423 (2016).

[26] A. Banerjee, J. Yan, J. Knolle, C. A. Bridges, M. B. Stone, M. D. Lumsden, D. G. Mandrus, D. A. Tennant, R. Moessner, and S. E. Nagler, arXiv:1609.00103.

[27] L. J. Sandilands, Y. Tian, K. W. Plumb, Y.-J. Kim, and K. S. Burch, Phys. Rev. Lett. **114**, 147201 (2015).

[28] K.-J. Ran, to be published.

[29] S. M. Winter, Y. Li, H. O. Jeschke, and R. Valentí, Phys. Rev. B **93**, 214431 (2016).

[30] H.-S. Kim and H.-Y. Kee, Phys. Rev. B **93**, 155143 (2016).

[31] R. Yadav, N. A. Bogdanov, V. M. Katukuri, S. Nishimoto, J. van den Brink, and L. Hozoi, arXiv:1604.04755.

[32] L. J. Sandilands, Y. Tian, A. A. Reijnders, H.-S. Kim, K. W. Plumb, Y.-J. Kim, H.-Y. Kee, and K. S. Burch, Phys. Rev. B **93**, 075144 (2016).

[33] Z.-Y. Dong and J.-X. Li, prepared.

[34] K. Li, S.-L. Yu, and J.-X. Li, New Journal of Physics **17**, 043032 (2015).

[35] H.-S. Kim, V. S. V., A. Catuneanu, and H.-Y. Kee, Phys. Rev. B **91**, 241110 (2015).

[36] Z.-Y. Dong, W. Wang, and J.-X. Li, to be published.

[37] Y. K. R. A. Muniz and C. D. Batista, Prog. Theor. Exp. Phys. , 083I01 (2014).
[38] X. Zhou, H. Li, J. A. Waugh, S. Parham, H.-S. Kim, J. A. Sears, A. Gomes, H.-Y. Kee, Y.-J. Kim, and D. S. Dessau, Phys. Rev. B **94**, 161106 (2016).
[39] H. Wang, S. L. Yu, and J. X. Li, Phys. Rev. B **91** (2015).
[40] S.-L. Yu, Z.-J. Yao, and J.-X. Li, Journal of Physics: Condensed Matter **27**, 505701 (2015).
[41] L.-Y. Xiao, S.-L. Yu, W. Wang, Z.-J. Yao, and J.-X. Li, EPL (Europhysics Letters) **115**, 27008 (2016).
[42] P. Giannozzi, S. Baroni, N. Bonini, M. Calandra, R. Car, C. Cavazzoni, D. Ceresoli, G. L. Chiarotti, M. Cococcioni, I. Dabo, A. Dal Corso, S. de Gironcoli, S. Fabris, G. Fratesi, R. Gebauer, U. Gerstmann, C. Gougoussis, A. Kokalj, M. Lazzeri, L. Martin-Samos, N. Marzari, F. Mauri, R. Mazzarello, S. Paolini, A. Pasquarello, L. Paulatto, C. Sbraccia, S. Scandolo, G. Sclauzero, A. P. Seitsonen, A. Smogunov, P. Umari, and R. M. Wentzcovitch, J. Phys. Condens. Matter **21**, 395502 (2009).
[43] N. Marzari and D. Vanderbilt, Phys. Rev. B **56**, 22 (1997).